

# SPARCS: A Sparse Recovery Approach for Integrated Communication and Human Sensing in mmWave Systems

Jacopo Pegoraro  
pegoraroja@dei.unipd.it  
University of Padova  
Padova, Italy

Michele Rossi  
michele.rossi@unipd.it  
University of Padova  
Padova, Italy

Jesus O. Lacruz  
jesusomar.lacruz@imdea.org  
IMDEA Networks Institute  
Madrid, Spain

Joerg Widmer  
joerg.widmer@imdea.org  
IMDEA Networks Institute  
Madrid, Spain

## ABSTRACT

A well established method to detect and classify human movements using Millimeter-Wave (mmWave) devices is the time-frequency analysis of the small-scale Doppler effect (termed micro-Doppler) of the different body parts, which requires a regularly spaced and dense sampling of the Channel Impulse Response (CIR). This is currently done in the literature either using special-purpose radar sensors, or interrupting communications to transmit dedicated sensing waveforms, entailing high overhead and channel utilization. In this work we present SPARCS, an integrated human sensing and communication solution for mmWave systems. SPARCS is the first method that reconstructs high quality signatures of human movement from irregular and sparse CIR samples, such as the ones obtained during communication traffic patterns. To accomplish this, we formulate the micro-Doppler extraction as a sparse recovery problem, which is critical to enable a smooth integration between communication and sensing. Moreover, if needed, our system can seamlessly inject short CIR estimation fields into the channel whenever communication traffic is absent or insufficient for the micro-Doppler extraction. SPARCS effectively leverages the intrinsic sparsity of the mmWave channel, thus drastically reducing the sensing overhead with respect to available approaches. We implemented SPARCS on an IEEE 802.11ay Software Defined Radio (SDR) platform working in the 60 GHz band, collecting standard-compliant CIR traces matching the traffic patterns of real WiFi access points. Our results show that the micro-Doppler signatures obtained by SPARCS enable a typical downstream application such as human activity recognition with more than 7 times lower overhead with respect to existing methods, while achieving better recognition performance.

## 1 INTRODUCTION

There is a growing interest in human tracking [38], Human Activity Recognition (HAR) [29] and person identification [40] using Millimeter-Wave (mmWave) devices, where the high carrier frequency and large available bandwidth allow for accurate Doppler estimation and precise localization and tracking. To fully exploit these properties, a large body of work has focused on dedicated mmWave radars, that adopt specifically designed frequency modulated transmissions to extract the micro-Doppler ( $\mu$ D) effect caused by human motion (a so-called  $\mu$ D signature) [27, 35].

At the same time, given the increasing number of mmWave network technologies such as 3GPP 5G-NR [34] and IEEE 802.11ad/ay [36, 37], Integrated Sensing And Communication (ISAC) solutions are highly appealing. They effectively repurpose communication devices by endowing them with additional environment sensing capabilities, thus avoiding the cost of installing dedicated radar hardware. This recent trend has led to the identification of sensing as a key feature of next generation 6G mobile networks [18] and the creation of the IEEE 802.11bf standardization group [26], aimed at enabling sensing features in Wireless Local Area Networks (WLANs). However, ISAC system designs are still very limited, focusing on joint communication and sensing waveform design [19], which would require significant modifications to existing communication protocols and a reduction in the achievable communication data rates. Other approaches [17, 18, 23, 39] need to alternate communication and sensing phases according to a time-division scheme, where regularly spaced, radar-like transmissions are performed during dedicated sensing periods. This is needed to perceive the fine-grained  $\mu$ D effect of human motion, for which dense and regular sampling of the Channel Impulse Response (CIR) is required, causing significant overhead and channel occupation.

In this paper, we address the problem of enabling ISAC in realistic mmWave communication systems, by reusing existing communication traffic for sensing as much as possible and thus introducing only a minimal amount of additional overhead. To this end, we propose SPARCS, the first mmWave ISAC system that reconstructs human  $\mu$ D signatures from *irregular and sparse* CIR samples obtained from realistic traffic patterns. The main insight of SPARCS is to leverage the intrinsic sparsity of the reflections in the mmWave channel to pose the  $\mu$ D reconstruction as a sparse recovery problem. Indeed, mmWave CIR estimation can naturally separate signal propagation paths with  $< 10$  cm resolution, leading to a sparse multi-path environment and consequently a sparse CIR in the Doppler domain. This allows obtaining highly accurate  $\mu$ D signatures from only a small, randomly distributed fraction of the CIR samples that are currently needed by existing ISAC methods. To do so, SPARCS first performs CIR resampling to construct a regular grid of CIR samples with missing values due to the irregularity of the sampling process in time. Next, a sparse reconstruction method is used to obtain the  $\mu$ D spectrum, decoupling different propagation paths to leverage their sparsity property. Lastly, whenever communication traffic is absent or insufficient for the  $\mu$ D extraction, SPARCS supports a

dynamic injection of very short CIR estimation fields into the (idle) channel. Given its sparse recovery capabilities, only a small number of additional CIR sensing units are needed to retrieve the  $\mu\text{D}$ , thus entailing a negligible overhead to the communication rate.

SPARCS is compatible with any mmWave system that supports transmit beamforming for directional communication and CIR estimation. This is the case, for example, for IEEE 802.11ay WLANs at 60 GHz, which provide in-packet CIR estimation for beam tracking purposes, and for 3GPP 5G-NR, where base stations can send frequent downlink CSI-Reference Signal (CSI-RS) to estimate the channel using different Beam Patterns (BPs).

To evaluate SPARCS' performance, we implement it on a 60 GHz IEEE 802.11ay Software Defined Radio (SDR) experimentation platform. We then test it on sparse and irregular CIR samples derived from standard-compliant traces, both for synthetic traffic and traffic patterns obtained from datasets of operational real-world WiFi Access Points (APs) deployments [25]. To assess the quality of the reconstructed  $\mu\text{D}$  signatures, we use them as input for a typical downstream task such as HAR, which classifies human movement detected by the captured  $\mu\text{D}$  into different possible activities. The main contributions of our work are summarized next.

- (1) We propose SPARCS, an ISAC method for mmWave systems that can reconstruct high-quality  $\mu\text{D}$  signatures of human movement from irregular and sparse CIR estimation samples. SPARCS reuses training fields appended to communication packets as sensing units, and injects additional sensing units if necessary, adapting to the underlying communication traffic and minimizing the sensing overhead.
- (2) We provide an original formulation of the  $\mu\text{D}$  extraction in communication systems as a sparse recovery problem, leveraging the intrinsic high distance resolution and sparsity properties of the mmWave channel. As a side effect, this also improves the quality of the resulting spectrograms, making them more robust to noise and interference.
- (3) We design and validate an algorithm to perform the injection of additional sensing units when communication traffic is insufficient. The process is dynamic, requires no knowledge about future packet transmissions, and incurs minimal overall overhead.
- (4) We evaluate SPARCS by implementing it on an IEEE 802.11ay-compliant 60 GHz SDR platform and testing it on CIR measurements collected with realistic WiFi traffic patterns. For the common HAR task, the  $\mu\text{D}$  signatures reconstructed by SPARCS achieve better F1 scores than existing methods, while reducing sensing overhead by a factor of 7.

The paper is organized as follows. In Section 2 we discuss the necessary preliminaries for mmWave human  $\mu\text{D}$  sensing using CIR. SPARCS is introduced and explained in detail in Section 3, describing the sparse recovery problem formulation and the involved processing steps. In Section 4 we discuss the implementation of SPARCS on an SDR platform, and Section 5 provides an evaluation of the system on real measurement traces. We summarize the related work in Section 6 and give concluding remarks in Section 7.

## 2 PRIMER ON MMWAVE SENSING

In this section we give a brief description of the CIR model for mmWave communication systems that we use for sensing. We then describe a baseline approach that allows tracking the movement of people in the environment and extract their  $\mu\text{D}$  signatures using *regularly sampled* CIR information. This forms the basis of our SPARCS design, which entirely *eliminates* the requirement of fixed Inter-Frame Spacing (IFS) and enables ultra low-overhead ISAC.

### 2.1 Sensing in mmWave systems

Capturing the movement features of humans in the environment requires an analysis of the reflections of the transmitted signal from their bodies, which is usually carried out applying signal processing techniques to the CIR. Due to the high path loss occurring at mmWave frequencies, directional communication is employed by means of transmitter and receiver beamforming, typically using phased antenna arrays. The transmitter and the receiver use suitable BP configurations of their antenna arrays to maximize the signal strength [11, 36, 37]. To successfully sense with a mmWave system, *at least* one of the BPs has to illuminate the subjects of interest, as only in this case the reflected signal carries detectable information about the movement signature. To this end, we consider a setup where an AP transmits packets and is able to collect the reflections of *its own* signal, after being reflected by objects (including humans). This reflection is collected by the receive array of the AP itself using a quasi-omnidirectional BP. This requires full-duplex capabilities, as is common in ISAC scenarios [14], which in the simplest form can be achieved with a Multiple Input Multiple Output (MIMO) system in a mixed configuration with one RF chain as transmitter and another as receiver. The CIR estimation fields used for sensing, which we denote by *sensing units*, can either be piggybacked by appending them as a trailer to the Physical Layer (PHY) communication packets or transmitted independently (*injected*). mmWave standards implement beam training mechanisms that help to establish a communication link by testing different BP combinations and then selecting the best one. Such functionality is supported by all mmWave standards. For example, 5G-NR [11], use Synchronization Signal Block (SSB) and CSI-RS for beam management, while WLAN systems adopting the IEEE 802.11ad/ay standards [36, 37] use channel estimation and training fields (CEF and TRN, respectively) to obtain accurate CIR information. Our framework to extract sensing information from CIR measurements can be applied regardless of the specifics of the standards.

### 2.2 mmWave CIR model

Due to the large transmission bandwidth of mmWave systems, channel measurements contain fine-grained information about the environment [18, 23, 39]. Depending on the communication system we consider, sensing could be performed using the 5G-NR Orthogonal Frequency Division Multiplexing (OFDM) Channel State Information (CSI), which contains the channel gains for each OFDM subcarrier, or the IEEE 802.11ad/ay Single Carrier (SC) CIR. Both communication schemes are suitable for human sensing: (i) in 5G-NR, the base stations can send frequent downlink CSI-RS to estimate the channel using different BPs, while (ii) in IEEE 802.11ay in-packet beam tracking is enabled, so that specific fields called

training fields (TRN), each using a different BP, can be appended to communication packets. In the following, we focus on SC CIR, and show how to extract the  $\mu$ D effect of human movement. However, previous works have demonstrated that similar processing can be performed with OFDM CSI [18, 20], and SPARCS is general enough to be applied in both cases.

We consider a multipath propagation environment with a time-varying number of reflectors,  $P(t)$ . These cause physical signal propagation paths that can be separated in the CIR according to a finite *ranging resolution*, i.e., the capability of the system to resolve the distance of the reflectors causing different signal paths. This is given by  $\Delta d = c/2B$ , where  $B$  is the transmitted signal bandwidth and  $c$  the speed of light. Thus, the CIR contains the complex channel gains for a discrete grid of possible signal paths (or *distance bins*), with indices  $\ell = 0, \dots, L-1$ . Each path is associated with a specific distance from the AP, according to the relation  $d_\ell = c\tau_\ell/2$ , with  $\tau_\ell$  being the delay associated with path  $\ell$ . Moreover, the CIR depends on the specific BP used during the transmission, denoted by  $b = 0, \dots, N_{\text{BP}} - 1$ . For carrier frequency  $f_o$ , the CIR along  $\ell$ , using BP  $b$  at time  $t$  is

$$h_{\ell,b}(t) = \sum_{p=1}^{P_\ell(t)} a_{\ell,b}^p(t) \exp \left\{ -j2\pi \frac{2f_o}{c} \left[ d_\ell + \int_0^t v_\ell^p(x) dx \right] \right\}. \quad (1)$$

In Eq. (1),  $P_\ell(t)$  is the number of physical reflectors whose contributions overlap in the  $\ell$ -th CIR path, as their distances are within  $d_\ell \pm \Delta d/2$ , while  $v_\ell^p$  is the radial velocity<sup>1</sup> of reflector  $p$ . The quantity  $a_{\ell,b}^p(t)$  is the complex gain due to the joint effect of the transmitter BP, the object reflectivity and the signal attenuation.

### 2.3 micro-Doppler extraction

The extraction of the  $\mu$ D spectrum from multiple, concurrently moving subjects requires tracking the position of each person in the physical space, in order to separate their individual contributions to the CIR. Then, a spectral analysis over different CIR samples yields the desired  $\mu$ D signature [13, 23].

**2.3.1 People tracking.** People tracking is performed by extracting measurements of each person's distance and angular position with respect to the AP across time, as detailed, e.g., in [23]. This process consists of (i) removing the background contribution to the CIR by subtracting the average CIR across a suitable time interval, (ii) selecting the locally strongest reflection paths in the CIR (peaks) and obtaining the corresponding distance  $d_\ell$ , (iii) computing the Angle of Arrival (AoA),  $\theta$ , of the reflection from the correlation between the different BPs gains and the strengths of the CIRs across the whole angular Field-of-View (FOV) [15]. The approach in (iii) requires the BP shapes to be estimated in advance, and is based on the intuition that different BPs illuminate different possible reflectors in the environment, depending on their position. Therefore, we can expect to receive the reflected signal from a certain subject only when a BP is pointing in his/her direction. The resulting set of distances and angles represent candidate positions of humans in the environment. A multi-target tracking method such as a Joint Probabilistic Data Association Filter (JPDAF) [2] allows smoothing the trajectories of the subjects by rejecting noise and clutter.

<sup>1</sup>By convention,  $v_\ell^p$  has a positive sign when the reflector moves away from the AP.

The tracking phase provides an estimate of the position of each subject, at every time instant  $t$ , which we denote by  $[\hat{d}(t), \hat{\theta}(t)]$  using symbol  $\hat{\cdot}$  to differentiate between our estimates and the true position. Due to step (ii) above, which selects the local peaks in the received power, typically only the reflections from the torso can be tracked when a person moves in the environment. In contrast, the head and the limbs cause much weaker reflections [35], whose contributions can only be detected in the  $\mu$ D spectrum. Nevertheless, tracking the spatial location of the torso is crucial for the  $\mu$ D extraction as it allows separating the contributions of the multiple subjects in the environment. Once  $\hat{d}(t)$  and  $\hat{\theta}(t)$  are determined, they are used to select the path  $\ell^*$  and the BP  $b^*$  that correspond to the distance and angular position of the subject, respectively. Then, the CIR waveform that contains the  $\mu$ D effect of the person's movement is  $h_{\ell^*,b^*}(t)$ . Besides enabling the separation of multiple subjects, this operation makes mmWave sensing systems much more robust to changes in the environment than sub-6 GHz systems [21]. While the latter are heavily affected by second-order reflections on walls and objects, mmWave sensing mostly relies on the line-of-sight path between the person and the transmitter/receiver, with little contribution from the external environment.

**2.3.2 micro-Doppler spectrum.** Human movement causes a small-scale Doppler effect on the reflected signal due to the different body parts, which possess different velocities and follow different trajectories [4]. This is referred to as  $\mu$ D effect and causes a measurable frequency modulation on the reflection. High frequency signals such as mmWave communications are particularly affected by the  $\mu$ D modulation due to their small wavelengths. Various techniques from time-frequency analysis can be applied to analyze the  $\mu$ D, obtaining *spectrograms* showing the time evolution of the signal energy contained in the different frequency bands of interest. The most popular and computationally efficient of such methods is the Short Time Fourier Transform (STFT) of  $h_{\ell,b}(t)$  [3], which consists in applying a windowed Fourier Transform (FT) on partially overlapping portions of the CIR. As shown in [13, 20, 23], STFT processing needs to be applied to a window of  $W$  subsequent estimates of the CIR with a *fixed* CIR sampling interval of  $T_c$  seconds, provided that the time spanned by the window is short enough to consider the movement velocity of the reflectors *constant* for its whole duration. Note that this operation allows detecting and separating the velocities of the  $P_\ell(t)$  reflectors, whose contributions overlap in path  $\ell$  when considering a single estimate of the CIR. The choice of  $T_c$  impacts the frequency resolution of the STFT,  $\Delta f^d = 1/(WT_c)$ , and its maximum measurable frequency,  $f_{\text{max}}^d = 1/(2T_c)$ . Using the relationship between the Doppler frequency and the corresponding velocity, one can obtain the velocity resolution and the maximum observable velocity as  $\Delta v = c/(2f_o WT_c)$  and  $v_{\text{max}} = c/(4f_o T_c)$ . To fully capture the range of velocities of interest for human movement, the typical approach is to select  $T_c$  such that  $v_{\text{max}}$  is sufficiently high that it covers the velocities that can occur in the human activities of interest, which may vary depending on the application [23, 29, 35].

Previous work assumes that the constraint of a fixed  $T_c$  is met, which does not hold in realistic communication scenarios, where packet transmissions are scheduled according to the needs of the

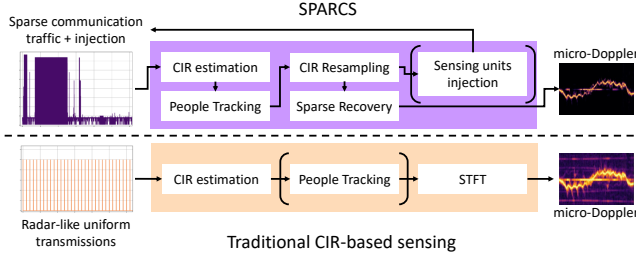


**Figure 1: Comparison between the traditional CIR-based human sensing and SPARCS.**

communication protocols rather than sensing accuracy. Traffic patterns are typically bursty and irregular and thus cannot be used by existing methods for human sensing. Instead, dedicated time slots need to be reserved for the transmission of sensing units, which is incompatible with the random access CSMA/CA MAC commonly used in IEEE 802.11. Conversely, SPARCS is the first approach that does not require any specific pattern in the transmission of the sensing units, enabling true ISAC by exploiting communication packets for sensing whenever possible, and introducing minimal additional overhead when necessary.

### 3 SPARCS METHODOLOGY

We now present the SPARCS algorithm to recover the  $\mu$ D spectrum from irregular and sparse CIR sampling patterns. The processing steps of SPARCS compared to traditional CIR-based sensing methods are shown in Fig. 1.

(1) **CIR resampling:** after CIR estimation and people tracking, for which we adopt the standard JPDAF technique [2], we apply a resampling strategy to approximate the irregularly spaced CIR values with a regular sequence whose sampling interval is chosen according to the desired  $\mu$ D resolution (Section 3.1). Due to irregularity of the original sampling process, the approximated regular sequence may contain missing values that need to be *filled* in the subsequent processing steps.

(2) **Sparse  $\mu$ D recovery:** we formulate the recovery of the  $\mu$ D spectrum from the incomplete CIR measurements as a sparse recovery problem. For this, we leverage two key aspects. On the one hand, the intrinsic sparsity of the mmWave channel leads to a small number of signal reflections from the human body that carry information about different body parts. On the other hand, the high distance resolution of mmWave systems makes the reflections from the different body parts separable. The combined effect of these two properties is that the resulting CIR is highly sparse in the Doppler frequency domain, as detailed in Section 3.2. We then solve the sparse recovery problem using the Iterative Hard Thresholding (IHT) algorithm for each CIR path (Section 3.3), and aggregate the results to obtain the final  $\mu$ D spectrum (Section 3.4).

(3) **Sensing unit injection:** when communication traffic is absent or too scarce to obtain an accurate reconstruction, our system can inject short sensing units into the (idle) channel to overcome the problem, as described in Section 3.5. Thanks to the sparse reconstruction of point (2), the amount of units that need to be injected is minimal and can be tuned to trade off between overhead and sensing accuracy.

### 3.1 CIR resampling

Our system samples the CIR at time instants  $t_i$ , which coincide with the reception of the reflections from the  $i$ -th transmitted packet. To reconstruct the  $\mu$ D spectrum from CIR samples which are randomly distributed in the time domain, we first resample the CIR to obtain regularly spaced samples with a fixed granularity  $T_c$ , where possible. To do so, we resort to the *slotted resampling* technique, which allows approximating a sequence of randomly spaced samples into a regular grid with *missing values* [1]. We consider  $N_s$  consecutive samples obtained at the time instants  $t_0, t_1, \dots, t_{N_s}$  and denote by  $0, T_c, 2T_c, \dots, (K-1)T_c$  the regular grid with step size  $T_c$ . Slotted resampling constructs a new CIR sample sequence  $h_{\ell,b}(kT_c)$  where the CIR values are obtained from the original sequence  $h_{\ell,b}(t_i)$  as follows. Time *bins* (or intervals) of length  $T_c$  are centered on each time instant of the regular grid, i.e., bin  $k$  is  $\beta_k = [kT_c - T_c/2, kT_c + T_c/2)$ , with center  $kT_c$ . Then, the value of the CIR corresponding to the  $k$ -th grid value is either (i) selected among the values of the original sequence whose sampling times fall inside bin  $k$ , taking the one whose sampling time is the closest to the bin center, or (ii) considered as a missing value if no samples of the original sequence fall inside bin  $k$ . Specifically,

$$h_{\ell,b}(kT_c) = \begin{cases} 0 & \text{if } \{t_i | t_i \in \beta_k\} = \emptyset, \\ h_{\ell,b}(t_k) & \text{otherwise,} \end{cases} \quad (2)$$

where the 0 values represent missing samples and

$$t_k = \arg \min_{\tau \in \{t_i | t_i \in \beta_k\}} |kT_c - \tau|. \quad (3)$$

The resulting, regularly spaced sequence of CIR samples is used to reconstruct the  $\mu$ D spectrum of the subject. However, due to the missing samples which are set to 0, a plain application of the STFT (as described in Section 2.3) would lead to a corrupted spectrum. In the next section we detail our solution to this problem, which is based on sparse recovery techniques.

### 3.2 Sparse $\mu$ D recovery problem formulation

Several methods exist to tackle the problem of computing the power spectrum of non-uniformly sampled signals [1]. Our approach belongs to the category of sparsity-based approaches, in which the sparsity of the signal in the frequency domain is leveraged to drastically reduce the number of measurements needed for an accurate reconstruction of the spectrum. We select windows of length  $W$  samples (window size) every  $\delta$  samples from the sequence  $h_{\ell,b}(kT_c)$ , choosing  $\delta = W/2$ . Due to the slotted resampling process, each window may contain missing samples. We denote by  $\mathcal{U}_m$  the set of indices of the available samples contained in the  $m$ -th window. Then, we define vector  $\mathbf{h}_{\ell,b}(m) \in \mathbb{C}^{|\mathcal{U}_m|}$ , containing the available CIR samples in the  $m$ -th window, and vector  $\tilde{\mathbf{h}}_{\ell,b}(m) \in \mathbb{C}^W$ , representing the complete  $m$ -th CIR window, which is only partially known due to the missing samples. We also denote by  $\mathbf{F}_{\text{inv}}$  the inverse Fourier matrix, whose element in position  $(g, l)$  is given by  $(\mathbf{F}_{\text{inv}})_{gl} = (1/\sqrt{W}) \exp(j2\pi gl/W)$ ,  $g, l = 0, \dots, W-1$  while  $\mathbf{U}_m = [\mathbf{u}_i^T]$ ,  $\forall i \in \mathcal{U}_m$  is the matrix that selects the rows of  $\mathbf{F}_{\text{inv}}$  whose indices are in  $\mathcal{U}_m$ .  $\mathbf{u}_i$  is the vector of all zeros but the  $i$ -th component, which equals 1.

The following relation holds between the incomplete CIR window,  $\mathbf{h}_{\ell,b}(m)$ , and the FT of the full CIR window,  $\mathbf{H}_{\ell,b}(m) \in \mathbb{C}^W$ ,

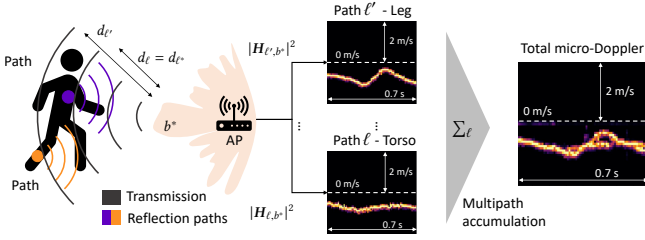


**Figure 2: Visual representation of the  $\mu$ D spectrum computed using SPARCS on 2 different CIR paths, one containing the reflection from a person’s torso, the other capturing the  $\mu$ D signature of the leg. The total  $\mu$ D is obtained summing together these contributions.**

which we aim to recover in order to compute the  $\mu$ D spectrum,

$$\mathbf{h}_{\ell,b}(m) = \mathbf{U}_m \tilde{\mathbf{h}}_{\ell,b}(m) = \mathbf{U}_m \mathbf{F}_{\text{inv}} \mathbf{H}_{\ell,b}(m) = \Psi_m \mathbf{H}_{\ell,b}(m), \quad (4)$$

where in the last step we use matrix  $\Psi_m = \mathbf{U}_m \mathbf{F}_{\text{inv}}$  as a shorthand notation. Given Eq. (4), our aim is to recover  $\mathbf{H}_{\ell,b}(m)$  from the incomplete measurement vector  $\mathbf{h}_{\ell,b}(m)$ , which is a typical sparse recovery or compressed sensing problem [7]. In this framework, it has been proven that recovering the FT of the desired signal is possible if the latter is sparse in the frequency domain, i.e., the FT only contains a low fraction of non-zero elements. To verify that this sparsity assumption holds in our case, we rewrite Eq. (1) after the resampling and windowing operations, so that the  $i$ -th sample of the complete  $m$ -th window is given by

$$\left[ \tilde{\mathbf{h}}_{\ell,b}(m) \right]_i = \sum_{p=1}^{P_\ell(m)} a_{\ell,b}^p(m) \exp \left\{ -j4\pi \frac{f_0}{c} \left[ d_\ell^p + (m\delta + i)T_c v_{\ell,m}^p \right] \right\}, \quad (5)$$

where  $v_{\ell,m}^p$  is the radial velocity of the  $p$ -th reflector in path  $\ell$  during window  $m$ , and  $d_\ell^p$  its distance from the AP. Here, we use the assumption from Section 2.3 that the velocity of each reflector can be considered constant during a window. In addition, we also consider that the reflective coefficients and the number of reflectors are constant. This is reasonable for the considered setup, where the reflectors are parts of the human body, which typically move slowly compared to the duration of a window  $WT_c$  (see also Section 4).

From Eq. (5), one can see that as long as  $P_\ell(m) \ll W$ , the FT of  $\tilde{\mathbf{h}}_{\ell,b}(m)$  is indeed sparse, as it is composed of  $P_\ell(m)$  spectral lines located at frequencies  $2f_0 v_{\ell,m}^p / c$ . Given the excellent distance resolution due to the high bandwidth of mmWave systems and the *intrinsic* sparsity and directionality of the channel, the different parts of the subject’s body tend to contribute to the  $\mu$ D spectrum in different CIR paths as shown in Fig. 2. Therefore,  $P_\ell(m)$  is generally close, if not equal, to 1. Sometimes the number of reflectors in a single path can be larger than 1, due to different body parts being closer than the distance resolution of the system, but this number is still much lower than  $W$ . This even holds for multiple subjects. Assume that two subjects with labels 1 and 2 are present in the monitored physical space, and denote by  $(\ell_1, b_1)$  and  $(\ell_2, b_2)$  their CIR path-BP pairs. According to Eq. (5), the sparsity assumption must hold for each pair *independently*, and this is verified as long as the subjects occupy different spatial positions. Specifically, (i) if  $\ell_1 \neq \ell_2$  the CIRs along BPs  $b_1$  and  $b_2$  are the combination of

### Algorithm 1 Single path sparse recovery.

**Input:**  $\mathbf{h}_{\ell,b^*}(m)$ ,  $\eta$ ,  $n_{\text{max}}$ ,  $\Omega$ ,  $\xi$ .

**Output:**  $\hat{\mathbf{H}}_{\ell,b^*}(m)$ .

- 1: Collect the set of available samples indices  $\mathcal{U}_m$ .
- 2: Build matrices  $\mathbf{U}_m = [\mathbf{u}_i^T]$ ,  $\forall i \in \mathcal{U}_m$  and  $\mathcal{F}_{\text{inv}}$ .
- 3: Compute  $\Psi_m = \mathbf{U}_m \mathcal{F}_{\text{inv}}$ .
- 4: Set  $\hat{\mathbf{H}}^{(0)} = 0$ ,  $n = 0$ ,  $\gamma^{(0)}$  to any value  $> \xi$ .
- 5: **while**  $n < n_{\text{max}}$  or  $\gamma^{(n)} > \xi$  **do**
- 6:    $\hat{\mathbf{H}}^{(n+1)} \leftarrow \text{Eq. (8)}$
- 7:    $\gamma^{(n+1)} \leftarrow \|\hat{\mathbf{H}}^{(n+1)} - \hat{\mathbf{H}}^{(n)}\|_2$
- 8:    $n \leftarrow n + 1$
- 9: **end while**
- 10: **return**  $\hat{\mathbf{H}}^{(n)}$

$P_{\ell_1}(m) \ll W$  and  $P_{\ell_2}(m) \ll W$  complex exponentials each, and (ii) if  $\ell_1 = \ell_2$ , but  $b_1 \neq b_2$ , the attenuation coefficient of  $b_1$  will mostly remove the reflection from subject 2 in  $\tilde{\mathbf{h}}_{\ell_1,b_1}$  and vice versa, making the contributions from the subjects separable. The contributions from different subjects overlap only if they occupy the same CIR path *and* share the same BP, which is very unlikely to occur in real cases due to the high distance ( $\sim 8$  cm) and angular (as low as  $2^\circ$ ) resolutions of the mmWave CIR [23]. Therefore, the sparsity assumption in SPARCS still holds even if multiple subjects are present in the environment. Due to this, we can assume that  $P_\ell(m) \ll W$  holds, and that sparse recovery techniques can be used to recover  $\mathbf{H}_{\ell,b}(m)$ , as detailed in the next section.

### 3.3 Single-path sparse recovery

Given the model from Eq. (4), the reconstruction of the CIR FT along each path can be posed as a sparse recovery problem. Specifically, we seek a vector  $\mathbf{H}_{\ell,b}(m)$  which is a solution to Eq. (4) while being as sparse as possible, coherent with the above discussion. Considering the BP  $b^*$  pointing in the direction of the target, the desired FT of  $\tilde{\mathbf{h}}_{\ell,b^*}(m)$  is the solution of the optimization problem

$$\mathbf{H}_{\ell,b^*}(m) = \arg \min_{\mathbf{H}} \|\mathbf{H}\|_0 \quad \text{s.t.} \quad \|\mathbf{h}_{\ell,b^*}(m) - \Psi_m \mathbf{H}\|_2 \leq \varepsilon, \quad (6)$$

where  $\|\cdot\|_0$  denotes the  $\ell_0$ -norm of a vector, i.e., the number of its non-zero components. The constant  $\varepsilon > 0$  can be estimated from the noise in the CIR, using a training dataset.

An approximate local solution to Eq. (6) can be found using fast greedy algorithms [7]. We adopt the IHT, which solves

$$\mathbf{H}_{\ell,b^*}(m) = \arg \min_{\mathbf{H}} \|\mathbf{h}_{\ell,b^*}(m) - \Psi_m \mathbf{H}\|_2^2 \quad \text{s.t.} \quad \|\mathbf{H}\|_0 \leq \Omega, \quad (7)$$

where  $\Omega$  is a pre-defined sparsity level parameter. The algorithm involves an iterative gradient descent step on the quadratic term in Eq. (7), followed by a thresholding operation:

$$\hat{\mathbf{H}}^{(n+1)} \leftarrow \mathcal{T}_\Omega \left[ \hat{\mathbf{H}}^{(n)} + \eta \Psi_m^T \left( \mathbf{h}_{\ell,b^*}(m) - \Psi_m \hat{\mathbf{H}}^{(n)} \right) \right], \quad (8)$$

where  $n$  is the iteration index and  $\mathcal{T}_\Omega$  is the hard-thresholding operator, which sets to 0 all the components of the argument vector except the  $\Omega$  largest ones in terms of the Euclidean norm.  $\eta$  is a learning rate parameter which can be tuned to improve the convergence properties. The iterative process is stopped whenever  $\|\hat{\mathbf{H}}^{(n+1)} - \hat{\mathbf{H}}^{(n)}\|_2 < \xi$  or when a maximum number of iterations,  $n_{\text{max}}$ , is reached. In SPARCS,  $\Omega$  is a key parameter, which is strictly related to the number of reflectors  $P_\ell(m)$ : as IHT reconstructs a vector which has at most  $\Omega$  non-zero elements,  $\Omega$  is an upper bound

for  $P_\ell(m)$ , and it can be thought of as the maximum number of reflectors per path that we allow reconstructing.  $\Omega$  can be tuned in order to obtain better  $\mu\text{D}$  reconstruction (see Section 5.5). The sparse recovery algorithm is summarized in Alg. 1. According to the compressive sensing theory [9], the reconstruction performance of IHT (and in general of any recovery algorithm) degrades as the number of available measurements,  $|\mathcal{U}_m|$ , decreases. Theoretical results show that the minimum number of measurements needed to reconstruct  $H_{\ell,b^*}(m)$  is  $O(\Omega \log(W/\Omega))$  [9], although the exact number has to be estimated empirically as it also depends on the level of noise present in the signal. In Section 5, we show that SPARCS can achieve excellent  $\mu\text{D}$  reconstruction with as few as  $W/8$  measurements per window, thanks to the high sparsity of the mmWave CIR.

### 3.4 Multi-path aggregation

The moving body of a person causes several reflections that affect more than one CIR path, as discussed in Section 3.2. Using the procedure described in the previous sections, SPARCS is able to retrieve the contribution of each path  $H_{\ell,b^*}(m)$  to the  $\mu\text{D}$ . Since the different body parts contribute to the  $\mu\text{D}$  in different paths, to fully capture human movement we need to combine the information from the different paths. Denote by  $Q$  the number of distance bins we aggregate to obtain the  $\mu\text{D}$  spectrum. For convenience we assume  $Q$  to be an odd integer, as this makes the following processing steps symmetric with respect to a central CIR path (corresponding to the torso), but the same steps can be applied for  $Q$  being even. We aggregate the spectra obtained from the path caused by the torso,  $\ell^*$ , with the  $\lfloor Q/2 \rfloor$  distance bins preceding  $\ell^*$  and the  $\lfloor Q/2 \rfloor$  subsequent distance bins, as they may contain the contributions of the other body parts. The expression of the total  $\mu\text{D}$  spectrum is

$$D(m) = \sum_{\ell=\ell^*-\lfloor Q/2 \rfloor}^{\ell^*+\lfloor Q/2 \rfloor} |H_{\ell,b^*}(m)|^2, \quad (9)$$

where the squared magnitude is applied element-wise. In addition, we apply normalization of the spectra in the range  $[0, 1]$  by computing  $D(m) \leftarrow \frac{D(m) - \min_i D_i(m)}{\max_i D_i(m) - \min_i D_i(m)}$ . Note that Eq. (9) entails solving  $Q$  optimization problems of the form in Eq. (7), however, the  $Q$  problems can be parallelized as they are completely independent. Decomposing the full  $\mu\text{D}$  spectrum reconstruction problem into  $Q$  subproblems effectively allows applying sparse recovery techniques, which in turn leads to a significant reduction of the number of measurements that are needed.

The value of  $Q$  is selected according to physical considerations and validated in practice, as described in Section 5. The  $\mu\text{D}$  vectors from Eq. (9) can be collected in sequences, one every  $\delta$  slots, forming  $\mu\text{D}$  spectrograms of arbitrary length, depending on the specific application that is being performed, e.g., activity recognition, fall detection, gait segmentation, etc. In the following, we refer to the number of  $\mu\text{D}$  vectors considered in such spectrograms as  $\Lambda$ .

### 3.5 Sensing unit injection

SPARCS can exploit the sensing units in sparsely distributed communication packets to recover the  $\mu\text{D}$  spectrum of human movement. However, during communication between the AP and one

---

#### Algorithm 2 Injection of sensing units in window $m$ .

---

**Input:**  $M_s$ .

- 1: # P1 - observation phase
- 2:  $N_a(m) \leftarrow$  no. of sensing units received in the first half of the window (either from reflected communications packets or injected).
- 3: # P2 - scheduling phase
- 4:  $N_w(m) \leftarrow \max(M_s - N_a(m), 0)$ .
- 5: Schedule  $\mathcal{S}_m = \{s_1, \dots, s_{N_w(m)}\}$ .
- 6: # P3 - transmission phase
- 7: **for**  $q = mW/2, \dots, (m+1)W/2 - 1$  **do**
- 8:   **if**  $q \in \mathcal{S}_m$  **then**
- 9:     **if** no reflected comm. packet received **then**
- 10:       Transmit the sensing unit.
- 11:        $\mathcal{S}_m \leftarrow \mathcal{S}_m \setminus \{q\}$ .
- 12:     **else**
- 13:       Use the sensing unit from the comm. packet
- 14:        $\mathcal{S}_m \leftarrow \mathcal{S}_m \setminus \{q\}$ .
- 15:     **end if**
- 16:   **else**
- 17:     **if** reflected comm. packet received **then**
- 18:       Use the sensing unit from the comm. packet
- 19:        $\mathcal{S}_m \leftarrow \mathcal{S}_m \setminus \{\min_{s \in \mathcal{S}_m} s\}$ .
- 20:     **end if**
- 21:   **end if**
- 22: **end for**

---

or more terminals it may happen that the AP remains silent for longer than the duration of a processing window,  $WT_c$ , or that the received packets are fewer than the minimum number of measurements required for an accurate  $\mu\text{D}$  reconstruction. In these cases, the sparse recovery algorithm can not recover  $H_{\ell,b}(m)$  as the available sensing units are insufficient. To tackle this problem, we allow our system to *inject* sensing units into the channel whenever the number of communication packets is not sufficient for Alg. 1 to work. Different from existing ISAC frameworks, our sparse recovery approach allows us to introduce a minimal amount of overhead, as the  $\mu\text{D}$  spectrum can be recovered from a number of CIR samples which is much lower than the full length of the window  $W$ . Note that for the injection of a sensing unit it is sufficient to transmit the necessary CIR estimation fields, without any preamble and header as used in conventional packets, since the unit is only received at the AP itself and contains a known waveform.

**3.5.1 Basis of the injection algorithm.** In the following, we present the proposed injection procedure assuming that both communication packets and sensing units are transmitted at times that lie on a uniform grid with spacing  $T_c$ . This simplification is valid due to the fact that the slotted resampling process described in Section 3.1 is used. Therefore, we can describe the injection process in terms of windows of size  $W$ , where each value in the window occupies a *slot* which is a multiple of  $T_c$ . Due to slotted resampling, the slots can be empty if no packet was transmitted sufficiently close to it.

Our approach consists in setting a minimum number of sensing units *per window*, termed  $M_s$ , that allows a sufficiently accurate reconstruction of the  $\mu\text{D}$  signatures. We then transmit additional units whenever the number of reflections of communication packets in the window is not sufficient to meet this minimum requirement. The proposed method only requires the knowledge of whether a reflected communication packet is received in the *current* slot, i.e., no information about the future traffic pattern is needed.

**3.5.2 Algorithm description.** The algorithm, summarized in Alg. 2, operates in three phases, namely *observation* (P1), *scheduling* (P2)

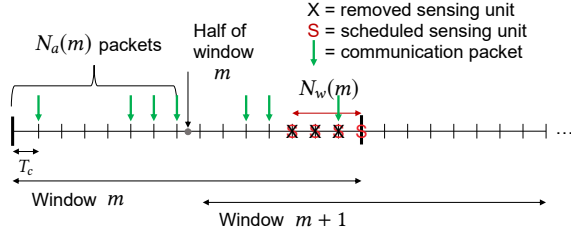


**Figure 3: Example injection procedure with  $M_s = 8, W = 16$ . 4 sensing units are scheduled after P1 and P2. Then, as three reflected communication packets are received, we reuse them and the first three scheduled sensing units are not transmitted. The fourth sensing unit is instead injected in the last slot.**

and *transmission* (P3). Recall that the  $\mu$ D extraction described in Section 3.2 follows a window-based approach, with subsequent windows overlapping by half of their length, as shown in Fig. 3. Consider a time instant between the end of window  $m - 1$  and the start of window  $m + 1$ . This coincides with the *half* of window  $m$ , which is between slots  $mW/2 - 1$  and  $mW/2$ . In this time instant we can observe how many reflected communication packets were received in the first half of window  $m$ , which spans the indices from  $(m - 1)W/2$  to  $mW/2 - 1$  (P1, line 2 in Alg. 2). We denote this number as  $N_a(m)$ . The injection algorithm is executed on a half-window basis at the time when window  $m - 1$  has ended and window  $m + 1$  has not yet started, as this allows reasoning on the sole current window  $m$ . Based on  $N_a(m)$ , we can compute how many sensing units we would need in the remaining half of window  $m$  in order to meet the requirement of at least  $M_s$  units, which we denote by  $N_w(m) = \max(M_s - N_a(m), 0)$ . However, the sensing process has no knowledge of when future communication packets will be received, so the best we can do is schedule the transmission of  $N_w(m)$  sensing units in the next half-window. The slots in which these packets are scheduled can be selected according to a deterministic rule or a probability distribution. We call  $\mathcal{S}_m = \{s_1, \dots, s_{N_w(m)}\}$  the set of indices of the slots in which we schedule the additional sensing units for the next half-window (P2, lines 4-5 in Alg. 2). While P1 and P2 are performed in a single time slot, before the second half of window  $m$  starts, P3 (lines 7-23 of Alg. 2) is a dynamic process that spans the whole second half of window  $m$ . The indices of the slots considered in this part of the algorithm are  $q = mW/2, \dots, (m + 1)W/2 - 1$ . Note that some communication packets, of which we have no knowledge, may be received in this second half-window. The procedure iterates over the slots and in each of them checks if a sensing unit was scheduled for that slot, i.e., if  $q \in \mathcal{S}_m$ . There are four possible cases:

- (1)  $q \in \mathcal{S}_m$  and no communication packet was received in this slot. In this case we transmit the sensing unit, then remove  $q$  from  $\mathcal{S}_m$ .
- (2)  $q \in \mathcal{S}_m$  and a communication packet (or more) was received in this slot. In this case we reuse the sensing unit in the communication packet and remove  $q$  from  $\mathcal{S}_m$ .
- (3)  $q \notin \mathcal{S}_m$  and no communication packet was received in this slot. In this case we just move to the next slot without taking action.
- (4)  $q \notin \mathcal{S}_m$  and a communication packet (or more) was received in this slot. In this case we reuse the sensing unit in the communication

packet, then we remove the next sensing unit from the scheduled ones, i.e., we set  $\mathcal{S}_m \leftarrow \mathcal{S}_m \setminus \{\min_{s \in \mathcal{S}_m} s\}$ .

Note that, despite operating on a half-window basis, due to the overlap of adjacent windows, our algorithm only poses a constraint on the minimum number of packets sent per *full* window. This means that half a window can be empty as long as enough sensing units are received in the other half.

**3.5.3 Scheduling the sensing units.** While the scheduling of the sensing units in P2 can be done with any arbitrary policy that guarantees that exactly  $N_w(m)$  packets are scheduled in the next half window, we want to maximize the number of sensing units that can be piggybacked on communication packets, rather than using a dedicated transmission. From P3 in Alg. 2, one can see that scheduling the sensing units towards the end of the half-window leaves more time for possible communication packets to become available and thus be reused instead of injecting a new sensing unit. Consequently, in SPARCS we schedule the sensing units for the second half of window  $m$  as a burst of packets spaced by  $T_c$ , which occupy the last  $N_w(m)$  slots of the window.

## 4 IMPLEMENTATION

In this section we describe the implementation of SPARCS on a mmWave SDR platform. We base our implementation on the IEEE 802.11ay WiFi protocol, as it operates in the unlicensed 60 GHz band and supports CIR estimation for different BPs.

**Testbed.** We use the open-source mm-FLEX experimentation platform from [15] for a baseline design. It has an FPGA-based baseband processor which can generate, capture and process (custom or standard compliant) frames with up to 1.76 GHz of bandwidth. The baseband processor is connected to mmWave RF front-ends with phased antenna arrays and supports various front-ends to operate in different frequency bands, e.g., at 28 GHz or 60 GHz [30]. In the remainder of this paper we use a 60 GHz RF front-end which simplifies experimentation as this is an unlicensed band, but we note that simply by changing the RF front-end, SPARCS can operate in a different band, e.g., for 5G-NR compatibility.

To implement SPARCS, we augment the functionalities of the testbed to enable full-duplex operation, not only in the baseband processor but also in the RF front-end. A block diagram of the system is shown in Fig. 4. In the baseband processor, the operation of the system is controlled by a state machine (SM) which triggers an AXI-DMA that reads the I/Q samples from the DDR-TX memory and feeds them to the DACs. The SM also triggers another AXI-DMA in the receiver datapath that saves the received samples in the DDR-RX memory, i.e., *both* datapaths are synchronized and no packet detection is required. To support the variable IFS extracted from real (or artificially generated) traces, we include a block RAM memory (BRAM) in the FPGA logic that stores the IFS that will be used in the experiments. The SM reads these values sequentially, introducing a delay in the system according to the value read from memory. The variable IFS functionality can be disabled at runtime to configure a *fixed* IFS. We remark that since we simultaneously use the up/down conversion stages from the *same* mmWave development kit, the Tx/Rx sub-systems are fed by the same local oscillator and thus the Carrier Frequency Offset (CFO) is very low ( $< 100$  Hz), which enables the extraction of the  $\mu$ D values required by SPARCS.

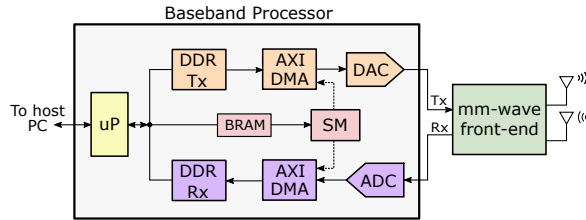


Figure 4: SPARCS implementation block diagram.

Table 1: Summary of the SPARCS implementation parameters. The suggested values based on experimental results are shown in bold.

System parameters		
Grid step	$T_c$	0.27 ms
Window length	$W$	64
Window shift	$\delta$	32
Sparsity parameter	$\Omega$	{1, 2, 3, 4, 5, 6, 7}
No. aggregated paths	$Q$	{1, 3, 5, 7, 9, 11, 13, 15}
Min. no. measurements	$M_s$	{4, 8, 16, 24, 32, 64}
IHT learning rate	$\eta$	1
IHT convergence threshold	$\xi$	$10^{-4}$
IHT maximum iteration number	$n_{\max}$	200

**IEEE 802.11ay CIR estimation details.** In IEEE 802.11ay, *in-packet* beam tracking [10] is introduced, where the CIR is estimated using different BPs *within a single packet*. This is implemented by appending a given number of training (TRN) fields to the packet. A TRN field is composed of 6 TRN *units* formed by complementary Golay sequences of 128 BPSK modulated samples, for a total of 768 samples [37]. In our implementation, we use  $n_{\text{TRN}}$  TRN fields as the SPARCS sensing unit, where each TRN field employs a different BP, and  $n_{\text{TRN}}$  is the number of subjects being tracked by the system, as a single TRN field per subject suffices. Considering the typical number of people that are to be simultaneously tracked in human sensing systems, reasonable  $n_{\text{TRN}}$  values range from 1 to 10. The CIR estimates obtained from the TRN fields are then used as the input to SPARCS sparse recovery algorithm.

**System parameters.** In Tab. 1 we summarize the system parameters used in the implementation. We set  $T_c = 0.27$  ms and  $W = 64$ , which lead to (i) a velocity resolution of  $\Delta v = c/(2f_o W T_c) \approx 0.14$  m/s and (ii) aliasing-free velocity measurements up to  $v_{\max} = \pm c/(4f_o T_c) \approx \pm 4.48$  m/s. These values are not critical to the functioning of our system, and can be modified according to specific implementation requirements. However, for reliable  $\mu\text{D}$  extraction without aliasing, it is advisable to adjust  $T_c$  to a value that allows capturing the range of velocities typically covered by human movement, e.g., approximately  $\pm 2-3$  m/s for a walking person, and up to  $\pm 5$  m/s for running or other fast movements [35]. Note that suitable values of  $T_c$  can also be obtained in 5G-NR systems, where a base station can transmit downlink CSI-RS frames with a periodicity between 0.3125 ms and 80 ms. For a 5G-NR carrier frequency of 28 GHz, using  $T_c = 0.3125$  ms leads to  $v_{\max} \approx \pm 8.57$  m/s, which is enough to capture fast human movement.

For people tracking, we use periodically transmitted in-packet beam training frames with 12 TRN units and antenna beams covering a FOV range from  $-45^\circ$  to  $45^\circ$ . Then, we utilize the distance and

AoA estimation procedure described in Section 2.3.1, as proposed in [23], to which we refer for further details. We experimented with different values of  $M_s$ ,  $\Omega$  and  $Q$ , as reported in Tab. 1 and described in Section 5.3 and Section 5.5, while for the IHT algorithm we selected the parameters that led to the most accurate convergence results on our experiments, i.e.,  $\eta = 1$ ,  $\xi = 10^{-4}$  and  $n_{\max} = 200$ .

## 5 EXPERIMENTAL RESULTS

We now present the experimental results obtained with our SPARCS testbed implementation. The experiments were performed in a laboratory of  $6 \times 7$  meters with a complex multi-path environment due to additional reflections caused by furniture, computers, screens, and a wide whiteboard.

### 5.1 Results on synthetic traces

As a first qualitative result we show the  $\mu\text{D}$  spectrograms obtained by SPARCS on randomly sampled CIRs of a walking subject (see Fig. 5). For this, we use synthetic traces, generated by measuring the CIR using a uniform sampling interval equal to  $T_c$ , and then setting to 0 a variable number of uniformly distributed values *per window* to simulate missing samples. This is a simplified case, as (i) the available (not removed) packets lie on a regular grid with spacing  $T_c$ , therefore no approximation error is introduced by slotted resampling, and (ii) samples are removed on a per window basis, so a minimum number of packets in each window is guaranteed. Still, this evaluation is useful to highlight the impact of increasing the sparsity level of the measurements for SPARCS compared to standard STFT [24]. In the results presented in this section, no packet injection is performed, as we aim to assess the impact of the number of measurements per window on the reconstructed  $\mu\text{D}$ . In Fig. 5b we show the baseline walking spectrogram obtained using the standard STFT using the full window of 64 samples, as done in [23]. The spectrogram shows a typical walking  $\mu\text{D}$  modulation, with the contribution of the static clutter (the strong component at 0 velocity), of the torso (the strong oscillating component around  $\pm 1.5$  m/s and the limbs (the faint contributions around the torso component). Moreover, a certain amount of noise and interference is present, as shown by the non-zero background level and the horizontal lines at around  $\pm 2$  m/s and  $\pm 3.7$  m/s. In Fig. 5c, the same method is applied to windows with only 16 out of 64 the samples retained, while the rest is set to 0. The impact is very strong as it completely corrupts the useful structure in the  $\mu\text{D}$  signature. From Fig. 5d to Fig. 5f we show the results obtained by SPARCS, on the same sequence, with 64, 16 and 4 samples out of 64, respectively. At the top of each figure, we report the Root Mean-Squared Error (RMSE) of the  $\mu\text{D}$  with respect to a ground truth spectrogram, shown in Fig. 5a. This ground truth was obtained from the STFT output with full measurement windows (Fig. 5b), by manually isolating the useful  $\mu\text{D}$  spectrum containing the gait information and setting to 0 any background noise and interference lines. We observe two interesting aspects. On the one hand, the SPARCS algorithm can successfully recover the  $\mu\text{D}$  spectrum even when a large fraction of the samples is missing, and the quality of the result decreases *gracefully* with the sparsity of the available measurements. Unlike standard STFT, SPARCS almost completely eliminates the noise and interference in the estimated  $\mu\text{D}$  spectrogram. Such improvement is



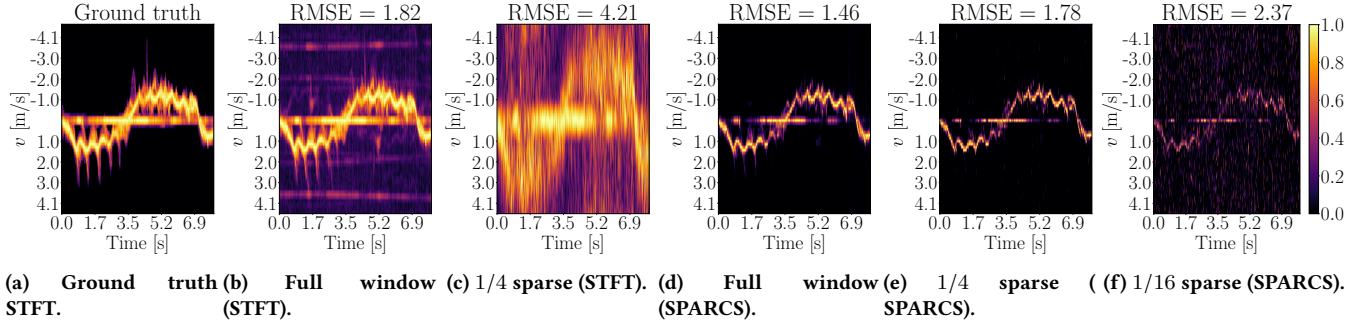


Figure 5: Walking  $\mu$ D spectrograms and RMSE for different levels of sparsity, obtained by uniformly removing samples for each window.

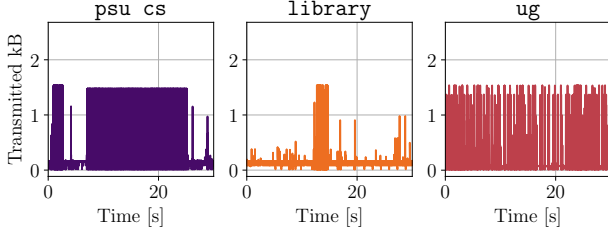


Figure 6: Example traffic patterns from the pdx/vwave dataset.

Table 2: Details of the 3 sequences of the pdx/vwave dataset.

Trace	Environment	No. frames	Duration
psu cs	University CS dept.	260326	1 : 00 h
library	Public library	1300671	4 : 00 h
ug	Coffee shop	895721	2 : 34 h

made possible by the sparsity constraint in Eq. (7), which allows for a lower RMSE than STFT operating on full measurement windows. This is the main reason why SPARCS not only reduces the overhead needed for human sensing, but also improves its accuracy.

## 5.2 Realistic traces: the pdx/vwave dataset

Next, we evaluate the performance of SPARCS on realistic WiFi AP traces. This poses an experimental challenge, because commercial devices implementing the IEEE 802.11ay standard are not yet available, and no public datasets containing real traffic traces for the PHY layer of mmWave WiFi (IEEE 802.11ay/ad) exist, to the best of our knowledge. For this reason, we used the pdx/vwave dataset, containing real traffic traces captured in different real environments from WiFi APs employing a legacy (sub-6 GHz) WiFi protocol [25]. Specifically, we use 3, over 1 hour long, traces from this dataset, called psu cs, library and ug, respectively. We select traces collected in different environments to represent different kinds of traffic patterns (see Tab. 2).

The pdx/vwave dataset includes information about the transmission instants and packet sizes of all packets outgoing from the considered AP. Exploiting this information, we perform our measurements transmitting packets according to these time patterns (see Section 5.3), using the BRAM in the FPGA to store the desired transmission instants (see Section 4). On top of the existing

pdx/vwave communication patterns we use the injection algorithm (Alg. 2) to send additional sensing units when needed.

Even though the pdx/vwave dataset is based on a legacy sub-6 GHz WiFi protocol, we argue that it is still reasonable to use it to obtain realistic packet transmission patterns. While in the pdx/vwave dataset the maximum physical layer PDU size is  $\text{PPDU}_{\text{pdx}} = 1.5$  kB (without packet aggregation), in IEEE 802.11ay three main transmission modes are defined, namely High Throughput (HT), Directional Multi Gigabit (DMG) and Very High Throughput (VHT), with maximum physical layer PDU sizes,  $\text{PPDU}_{\text{ay}}$ , of 65 kB, 262 kB and 4692 kB, respectively [36, 37]. With the increase in the packet sizes, the data rates of mmWave systems have increased accordingly, and in IEEE 802.11ay they will range from 0.3 Gbps to several Gbps. As a numerical example, the traffic patterns in pdx/vwave with a typical bitrate of 4 Mbps would correspond to a bitrate of 0.7 Gbps in DMG IEEE 802.11ay when using an aggregated packet size of 262 kB instead of 1.5 kB. Note that traces with a larger number of packets and smaller PDU sizes (as will likely be the case in real deployments) will simply increase the sensing accuracy and further reduce the overhead.

## 5.3 Human activity recognition results

To evaluate the quality of the  $\mu$ D spectrograms extracted by SPARCS, we use them as the input to a HAR method. Specifically, we follow a standard approach, training a deep neural network on a dataset of  $\Lambda \times W$  dimensional  $\mu$ D spectrograms, with  $\Lambda = 200$  (equivalent to  $\approx 1.76$  s), in order to classify the movement performed by the person during that time. In order to provide a comparison with other IEEE 802.11ay HAR methods based on regular CIR sampling, such as RAPID [23], we consider the 4 following activities: walking, running, sitting and waving hands. For HAR, we use a standard Convolutional Neural Network (CNN) architecture, composed of 4 *inception modules* [33] performing  $1 \times 1$ ,  $3 \times 3$  and  $5 \times 5$  convolutions. The number of filters used is 8, 16, 32 and 64 for the 4 modules, respectively. The convolutional blocks are followed by a fully-connected layer with 64 neurons, to which we apply Dropout [31], and a final Softmax layer with 4 outputs [12]. We use the *exponential-linear unit* activation function after each layer [6].

*5.3.1 Training data.* We collected a training dataset involving 6 different subjects performing the 4 activities, for a total duration of about 12 minutes each. This leads to over 400 partially overlapping, 1.76 s long,  $\mu$ D sequences per activity, which we then augmented

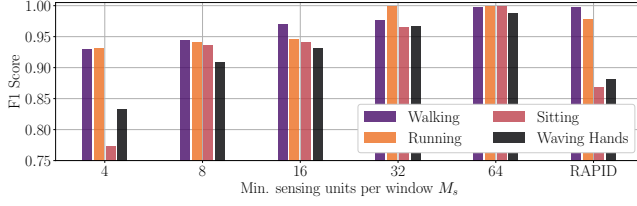


Figure 7: Per-class F1 scores obtained by SPARCS (for different values of  $M_s$ ) and RAPID on our test dataset [23].

as described shortly. Note that the training data only includes *uniformly sampled* CIR traces with sampling period  $T_c = 0.27$  ms. The CNN training is done for 80 epochs, using a learning rate of  $10^{-4}$ , the Adam optimizer and the cross-entropy loss function [12]. In order to enhance the robustness of the CNN, we apply an ad-hoc data augmentation strategy: we randomly remove some of the CIR samples in each window of the training dataset, and then apply SPARCS’ IHT algorithm to reconstruct the spectrograms (see Section 5.1). We repeat the process using a sparsity level of  $1/8$ ,  $1/4$  and  $1/2$ , enlarging the training dataset to 4 times its original size, for a total of approximately 1600  $\mu$ D spectrograms per activity. A randomly selected subset of the training data (around 10 %) was used as a validation set to tune the CNN hyperparameters.

**5.3.2 Test data.** We test the CNN on the  $\mu$ D spectrograms obtained from CIR samples collected using the pdx/vwave packet traces described in Section 5.2. We collect four, randomly selected, 20 s long traces (one per activity) for each of the 3 sequences types (psu cs, library and ug). We repeat the experiments for different values of the minimum number of sensing units per window,  $M_s = 4, 8, 16, 32, 64$ , for a total of 60 test sequences. The test data involves a single subject, which was not included in the training set.

**5.3.3 HAR F1 score.** We evaluate the performance of the CNN with the *per-class* F1 score metric [5], which effectively summarizes the precision and recall and preserves the class-specific results. Fig. 7 shows the total average per-class F1 score over the 60 sequences, for different values of the minimum number of sensing units per window,  $M_s$ . As a baseline for comparison, we also report the F1 score obtained by the RAPID algorithm from [23], which extracts the  $\mu$ D signatures by regularly sampling the CIR. Our results show that SPARCS can reach over 0.9 F1 scores on all activities with  $M_s = 8$  already, which corresponds to only  $1/8$  of the full measurements per window affects significantly only the ‘Sitting’ and ‘Waving hands’ activities, which involve fine-grained movements and are therefore more difficult to classify. Finally, we compare the results from SPARCS and RAPID [23]. For a fair comparison, we implemented RAPID’s STFT to extract the  $\mu$ D and trained the CNN on the resulting spectrograms without enlarging the dataset using different levels of sparsity described in the previous section. Instead, we directly use the training procedure of [23], since we found that the sparsity-based data augmentation slightly reduced RAPID’s performance. It can be seen that SPARCS’ sparse recovery problem formulation (Section 3.2) and enforcing a sparsity constraint on the individual paths is beneficial to HAR performance. The gap is

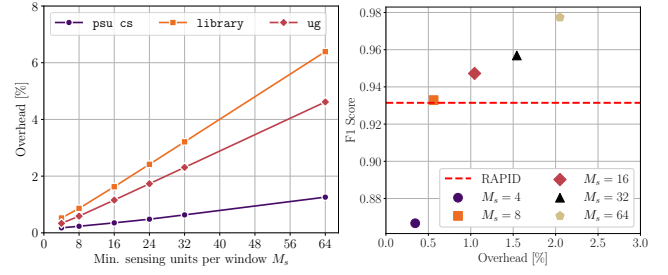


Figure 8: Overhead of SPARCS for different values of  $M_s$  in the three traces of the pdx/vwave dataset (left). Overhead vs. average HAR F1 score for different values of  $M_s$  (right).

particularly significant for ‘Sitting’ and ‘Waving hands’ as they involve lower energy traces in the spectrograms; these are more easily corrupted by noise and interference, that SPARCS is mostly able to reject (see, again, the comparison between Fig. 5b and Fig. 5d).

## 5.4 Overhead analysis

Increasing  $M_s$  to improve the HAR performance also increases the overhead of SPARCS. A first general measure of this can be obtained comparing the maximum size of a PPDU in IEEE 802.11ay to the size of a sensing unit. Recalling the three different modes introduced in Section 5.2 and the size of an IEEE 802.11ay TRN field (768 bits), we obtain that a sensing unit, with  $n_{\text{TRN}} = 1$ , is 0.1%, 0.03% and 0.002% of a PPDU in HT, DMG and VHT, respectively. Moreover, the channel occupation time for a sensing unit with  $n_{\text{TRN}} = 1$  is 436 ns [37], which is a negligible fraction (0.16%) of a slot of duration  $T_c$ .

Next, to evaluate the overhead of SPARCS on a realistic communication scenario, we use the traces of the pdx/vwave dataset. In this way, we can also assess the impact of injecting sensing units, as they are not useful to the communication process. Denote by  $c_i$  the number of bits in the  $i$ -th communication packet transmitted in the trace. As the number of bits transmitted in each trace refers to a legacy, lower bitrate, WiFi protocol, we rescaled the packet sizes according to the maximum PHY layer packet size in IEEE 802.11ay. We rescaled the size of packet  $i$  in each trace as  $\tilde{c}_i = (\text{PPDU}_{\text{ay}}/\text{PPDU}_{\text{pdx}}) \times c_i$ , with  $\text{PPDU}_{\text{ay}} = 262$  kB. We call  $n_c$  the number of transmitted communication packets in a trace, by  $\text{TRN}_{\text{len}}$  the length, in bits, of a piggybacked or injected TRN field,  $n_{\text{inj}}$  the number of injected sensing units and  $n_{\text{TRN}}$  the number of TRN fields used in every sensing operation (we consider it fixed, whereas in reality it is determined by the number of subjects in the environment). We define the overhead as a function of  $n_{\text{inj}}$  as

$$\text{OH}(n_{\text{inj}}) = \frac{n_{\text{TRN}} (n_c + n_{\text{inj}}) \text{TRN}_{\text{len}}}{\sum_{i=1}^{n_c} \tilde{c}_i}. \quad (10)$$

In Fig. 8, left, we show the overhead obtained on each of the three pdx/vwave traces, using  $n_{\text{TRN}} = 1$ . The overhead for different values of  $n_{\text{TRN}}$  can be obtained by using it as a multiplicative factor on the values in Fig. 8. We see that the overhead scales almost linearly as  $M_s$  is increased from 4 to 64. For values of  $M_s < 32$ , the entailed overhead is less than 4%, falling below 1% for  $M_s = 8$ . As a reference, we report the overhead for  $M_s = 64$ , which is the

value obtained by injecting sensing units continuously into the channel, piggybacking them eventually on communication packets if possible. Note that existing approaches requiring uniform CIR sampling, like RAPID [23], would require an even higher overhead, as not only do they need 64 samples per window, but these samples have to be regularly spaced as no resampling procedure is carried out. This means they would have to take precedence over potential data packets so that they are sent exactly at the right sampling time.

From Fig. 8, right, one can see that SPARCS can achieve an F1 score of over 0.9 for every activity for a minimum of  $M_s = 8$  sensing units per window, resulting in a sensing overhead of less than 1%. With this configuration, SPARCS achieves a better F1 score than existing approaches, while reducing overhead by a factor of 7 and being compatible with random access MAC protocols.

### 5.5 Sensitivity to the choice of the parameters

In Fig. 9, we show the effect of varying parameters  $Q$ , representing the number of paths aggregated around the person’s position (see Eq. (9)), and  $\Omega$ , which is the maximum number of resolvable Doppler components, equal to the sparsity parameter in the IHT algorithm. We computed the HAR per-class F1 score using a random subset of the 60 test sequences. The values adopted in our experiments are reported in Tab. 1.

**5.5.1 Impact of changing  $Q$ .** Our results show that SPARCS is robust to almost any value of  $Q$  when considering walking and running, whereas sitting and waving hands are negatively affected by reducing  $Q$  below 7. This is due to the fact that while walking and running are, in most cases, distinguishable even from the sole contribution of the torso, this is not true for sitting and waving hands that require including the reflection paths coming from the limbs. Computational complexity considerations are also in order for high values of  $Q$ , as it leads to solving  $Q$  times Eq. (7) at each  $\mu$ D extraction process. As the problems are independent, they can be solved in parallel, and thus a reasonable approach is to tune  $Q$  according to a trade-off between  $\mu$ D reconstruction accuracy and hardware resource availability for parallelization. In the following, we use  $Q = 9$ . Considering that we use  $B = 1.76$  GHz transmission bandwidth (1 IEEE 802.11ay channel), the range resolution of SPARCS is  $c/2B = 8.5$  cm. This means that summing the contribution of  $\lfloor Q/2 \rfloor$  distance bins before and after the one corresponding to the torso, we include in the spectrum a region of  $\pm 34$  cm around the person’s position, which is a reasonable value considering typical body sizes and that the subjects are moving.

**5.5.2 Impact of changing  $\Omega$ .** Fixing  $Q = 9$ , in Fig. 9 (right), we show that the best values for  $\Omega$  are 2 and 3 for all the activities. This is because using  $\Omega = 1$  often leads to only reconstructing the 0 Doppler component in the spectrogram, losing the information on the person’s movement. On the other hand, choosing  $\Omega$  too high makes the IHT reconstruction imprecise, as with a low number of measurements per window enforcing more sparsity is beneficial to restrict the number of possible solutions to Eq. (7).

## 6 RELATED WORK

**Dedicated mmWave radars.** The high sensitivity of mmWaves to micro-Doppler shifts, together with Deep Learning (DL) methods

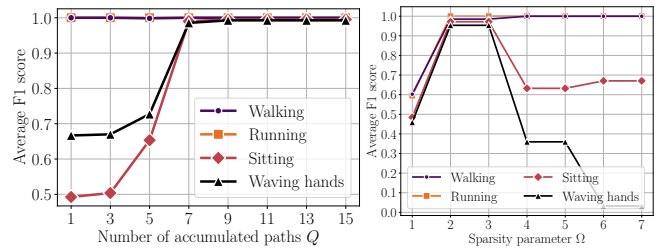


**Figure 9: Per-class F1 scores aggregating a different number of paths  $Q$  (left) and changing  $\Omega$ , the IHT sparsity parameter (right).**

for spectrogram analysis and classification, have been widely exploited to enable applications such as activity recognition [16, 29], person identification [21, 24] and bio-mechanical gait analysis [27]. The typical approach in these works is to transmit sequences of large bandwidth signals (of 2 to 4 GHz), with a rate dictated by the desired sensing resolution [22]. Thus, mmWave radar sensors have two main drawbacks:

- (i) they are specifically tailored to sensing and cannot perform communication. Moreover, their deployment cost is relatively high as one single sensor can reliably cover a range of at most 8 – 10 m due to the radial distortion and occlusion problems [8]. For this reason, ad-hoc radar sensor networks would need to be deployed in practical scenarios. Our method, in contrast, fully exploits existing mmWave communication systems with no modifications to the CIR estimation process or packet structures.
- (ii) The fixed chirp transmission interval, which is related to the  $\mu$ D resolution, requires regular transmissions with continuous channel occupation. Some works have explored the possibility of randomly subsampling the chirp transmission intervals using compressive sensing [7] to either save computational resources [32] or reduce the effect of unwanted interference [28]. However, these works are based on a radar framework, where the transmission instants can be freely chosen and optimized. SPARCS, instead, reuses the given underlying communication traffic as much as possible and only injects small additional sensing units when necessary.

**60 GHz WiFi sensing.** Research interest towards sensing with WiFi devices working in the mmWave band has mostly focused on the 60 GHz IEEE 802.11ad/ay standards [23, 38, 39]. These works target various applications, such as person tracking and gesture recognition, exploiting CIR estimation to detect humans in the environment. However, they require dedicated and regular sensing signal transmissions in order to function properly, entailing a significant overhead and channel utilization for sensing.

Our work significantly improves over the above mentioned studies in that it enables the reuse of randomly distributed communication packets via sparse recovery, whenever possible. This is of key importance to *integrate* sensing capabilities in communication devices while maintaining low overhead and complexity.

**Integrated sensing and communication.** A number of technical works address ISAC systems in next generation 5G/6G cellular networks [17, 18] and WLANs [23, 26]. Many of those target the joint communication and sensing waveform design [19] and are mostly oriented to automotive applications to measure distance and velocity of nearby vehicles. In contrast, few works focus on

human sensing [17], which is the aim of the present work. All of the above approaches alternate communication and sensing phases according to a time-division scheme, causing significant overhead and channel occupation. SPARCS instead, provides a full ISAC scheme, as it passively exploits communication traffic while dynamically injecting sensing units to cover silent periods. As a result, our method significantly reduces sensing overhead while at the same time improving the sensing accuracy.

## 7 CONCLUDING REMARKS

In this paper, we have designed and implemented SPARCS, the first mmWave ISAC system that can sense human  $\mu$ D signatures from irregular and sparse CIR estimates. These are obtained in a standard compliant way by both reusing optional CIR estimation fields appended to communication packets and sporadically injecting sensing packets whenever communication traffic is absent. Differently from the existing ISAC methods, SPARCS is based on a sparse recovery approach to the  $\mu$ D reconstruction, which is theoretically grounded in the intrinsic sparse multi-path environment of the mmWave channel. This enables an accurate  $\mu$ D extraction from a significantly lower number of randomly distributed CIR samples, thus drastically reducing the sensing overhead. After a CIR resampling step along the time domain, SPARCS performs an iterative sparse reconstruction in the frequency domain, decoupling different propagation paths at first, to leverage their sparsity property, and then combining them to obtain the final  $\mu$ D spectrum.

While SPARCS is compatible with different mmWave systems (e.g., 3GPP 5G-NR, and IEEE 60 GHz WLANs), for our implementation we used an IEEE 802.11ay SDR platform working in the 60 GHz band. We tested our system on a large set of standard-compliant CIR traces matching the traffic patterns of real WiFi access points, performing a typical downstream application such as HAR. Our results show that SPARCS entails over 7 times lower overhead compared to prior methods, while achieving better performance.

Future research directions include refining SPARCS by leveraging an exchange of information between the sensing and communication processes, e.g., utilizing sensing to optimize the beam selection, and exploiting communications for collaborative sensing.

## ACKNOWLEDGMENTS

This research work was sponsored in part by the European Union’s Horizon 2020 research and innovation programme under grants No. 871249, on “LOCALization and analytics on-demand embedded in the 5G ecosystem for Ubiquitous vertical applications” (LOCUS) and No. 861222, on “Millimeter-wave NeTworking and Sensing for beyond 5G” (MINTS), by the Spanish Ministry of Science and Innovation (MICIU) grant RTI2018-094313-B-I00 (PinPoint5G+), by the Region of Madrid through TAPIR-CM (S2018/TCS-4496) and by the Italian Ministry of Education, University and Research (MIUR) through the initiative “Departments of Excellence” (Law 232/2016).

## REFERENCES

- [1] Prabhu Babu and Petre Stoica. 2010. Spectral analysis of nonuniformly sampled data—a review. *Digital Signal Processing* 20, 2 (Mar 2010), 359–378.
- [2] Yaakov Bar-Shalom, Fred Daum, and Jim Huang. 2009. The probabilistic data association filter. *IEEE Control Systems Magazine* 29, 6 (2009), 82–100.
- [3] Boualem Boashash. 2015. *Time-frequency signal analysis and processing: a comprehensive reference*. Academic press.
- [4] Victor C Chen, Fayin Li, S-S Ho, and Harry Wechsler. 2006. Micro-Doppler effect in radar: phenomenon, model, and simulation study. *IEEE Transactions on Aerospace and Electronic Systems* 42, 1 (2006), 2–21.
- [5] Nancy Chinchor. 1992. MUC-4 Evaluation Metrics. In *Proceedings of the 4th Conference on Message Understanding (McLean, Virginia) (MUC4 '92)*. Association for Computational Linguistics, USA, 22–29.
- [6] Djork Arné Clevert, Thomas Unterthiner, and Sepp Hochreiter. 2016. Fast and accurate deep network learning by exponential linear units (ELUs). In *International Conference on Learning Representations (ICLR)*. San Juan, Puerto Rico.
- [7] Yonina C Eldar and Gitta Kutyniok. 2012. *Compressed sensing: theory and applications*. Cambridge University Press.
- [8] Lipeng Feng, Shibo Du, Zhen Meng, Anfu Zhou, and Huadong Ma. 2020. Evaluating mmWave Sensing Ability of Recognizing Multi-people Under Practical Scenarios. In *International Conference on Green, Pervasive, and Cloud Computing*. Springer, 61–74.
- [9] Simon Foucart and Holger Rauhut. 2013. *A Mathematical Introduction to Compressive Sensing*. Springer.
- [10] Y. Ghasempour, C. R. C. M. da Silva, C. Cordeiro, and E. W. Knightly. 2017. IEEE 802.11ay: Next-Generation 60 GHz Communication for 100 Gb/s Wi-Fi. *IEEE Communications Magazine* 55, 12 (2017), 186–192.
- [11] Marco Giordani, Michele Polese, Arnab Roy, Douglas Castor, and Michele Zorzi. 2018. A tutorial on beam management for 3GPP NR at mmWave frequencies. *IEEE Communications Surveys & Tutorials* 21, 1 (2018), 173–196.
- [12] Ian Goodfellow, Yoshua Bengio, and Aaron Courville. 2016. *Deep learning*. MIT press.
- [13] Belal Korany, Hong Cai, and Yasamin Mostofi. 2020. Multiple People Identification Through Walls Using Off-the-Shelf WiFi. *IEEE Internet of Things Journal* 8, 8 (2020), 6963–6974.
- [14] Preeti Kumari, Junil Choi, Nuria González-Prelcic, and Robert W Heath. 2017. IEEE 802.11 ad-based radar: An approach to joint vehicular communication-radar system. *IEEE Transactions on Vehicular Technology* 67, 4 (2017), 3012–3027.
- [15] Jesus O. Lacruz, Dolores Garcia, Pablo Jiménez Mateo, Joan Palacios, and Joerg Widmer. 2020. mm-FLEX: An Open Platform for Millimeter-Wave Mobile Full-Bandwidth Experimentation. In *Proceedings of the 18th International Conference on Mobile Systems, Applications, and Services (Toronto, Ontario, Canada) (MobiSys '20)*. Association for Computing Machinery, New York, NY, USA, 1–13. <https://doi.org/10.1145/3386901.3389034>
- [16] Guoji Lai, Xin Lou, and Wenbin Ye. 2021. Radar-Based Human Activity Recognition With 1-D Dense Attention Network. *IEEE Geoscience and Remote Sensing Letters* (2021).
- [17] Guoliang Li, Shuai Wang, Jie Li, Rui Wang, Fan Liu, Meihong Zhang, Xiaohui Peng, and Tony Xiao Han. 2021. Rethinking the Tradeoff in Integrated Sensing and Communication: Recognition Accuracy versus Communication Rate. *arXiv preprint arXiv:2107.09621* (2021).
- [18] Fan Liu, Yuanhao Cui, Christos Masouros, Jie Xu, Tony Xiao Han, Yonina C Eldar, and Stefano Buzzi. 2021. Integrated sensing and communications: Towards dual-functional wireless networks for 6G and beyond. *arXiv preprint arXiv:2108.07165* (2021).
- [19] Fan Liu, Longfei Zhou, Christos Masouros, Ang Li, Wu Luo, and Athina Petropulu. 2018. Toward dual-functional radar-communication systems: Optimal waveform design. *IEEE Transactions on Signal Processing* 66, 16 (2018), 4264–4279.
- [20] Francesca Meneghello, Domenico Garlisi, Nicolò Dal Fabbro, Ilenia Tinnirello, and Michele Rossi. 2021. Environment and Person Independent Activity Recognition with a Commodity IEEE 802.11 ac Access Point. *arXiv preprint arXiv:2103.09924* (2021).
- [21] Zhen Meng, Song Fu, Jie Yan, Hongyuan Liang, Anfu Zhou, Shilin Zhu, Huadong Ma, Jianhua Liu, and Ning Yang. 2020. Gait Recognition for Co-Existing Multiple People Using Millimeter Wave Sensing. In *AAAI Conference on Artificial Intelligence*. New York, New York, USA.
- [22] Sujeet Milind Patole, Murat Torlak, Dan Wang, and Murtaza Ali. 2017. Automotive radars: A review of signal processing techniques. *IEEE Signal Processing Magazine* 34, 2 (Mar 2017), 22–35.
- [23] Jacopo Pegoraro, Jesus Omar Lacruz, Enver Bashirov, Michele Rossi, and Joerg Widmer. 2021. RAPID: Retrofitting IEEE 802.11 ay Access Points for Indoor Human Detection and Sensing. *arXiv preprint arXiv:2109.04819* (2021).
- [24] Jacopo Pegoraro, Francesca Meneghello, and Michele Rossi. 2021. Multiperson Continuous Tracking and Identification From mm-Wave Micro-Doppler Signatures. *IEEE Transactions on Geoscience and Remote Sensing* 59, 4 (2021), 2994–3009.
- [25] Caleb Phillips and Suresh Singh. 2009. CRAWDDAD dataset pdx/vwave (v. 2009-07-04). Available at [https://crawdadd.org/pdx/vwave/20090704/wlan\\_nano\\_fcs](https://crawdadd.org/pdx/vwave/20090704/wlan_nano_fcs).
- [26] Francesco Restuccia. 2021. IEEE 802.11bf: Toward Ubiquitous Wi-Fi Sensing. *arXiv:2103.14918*
- [27] Ann-Kathrin Seifert, Moeness G Amin, and Abdelhak M Zoubir. 2019. Toward unobtrusive in-home gait analysis based on radar micro-Doppler signatures. *IEEE Transactions on Biomedical Engineering* 66, 9 (2019), 2629–2640.
- [28] Ervin Sejdić, Irena Orović, and Srđjan Stanković. 2018. Compressive sensing meets time–frequency: An overview of recent advances in time–frequency processing

- of sparse signals. *Digital signal processing* 77 (2018), 22–35.
- [29] Akash Deep Singh, Sandeep Singh Sandha, Luis Garcia, and Mani Srivastava. 2019. Radhar: Human activity recognition from point clouds generated through a millimeter-wave radar. In *Proceedings of the 3rd ACM Workshop on Millimeter-wave Networks and Sensing Systems*. 51–56.
- [30] Sivers Semiconductors. 2021. *Evaluation Kits*. <https://www.sivers-semiconductors.com/sivers-wireless/evaluation-kits/>.
- [31] Nitish Srivastava, Geoffrey Hinton, Alex Krizhevsky, Ilya Sutskever, and Ruslan Salakhutdinov. 2014. Dropout: a simple way to prevent neural networks from overfitting. *Journal of machine learning research* 15, 1 (Jun 2014), 1929–1958.
- [32] Srdjan Stanković, Irena Orović, Tamara Pejaković, and Miloš Orović. 2014. Compressive sensing reconstruction of signals with sinusoidal phase modulation: application to radar micro-Doppler. In *2014 22nd Telecommunications Forum Telfor (TELFOR)*. IEEE, 565–568.
- [33] Christian Szegedy, Wei Liu, Yangqing Jia, Pierre Sermanet, Scott Reed, Dragomir Anguelov, Dumitru Erhan, Vincent Vanhoucke, and Andrew Rabinovich. 2015. Going deeper with convolutions. In *Proceedings of the IEEE conference on computer vision and pattern recognition*. Boston, Massachusetts, USA.
- [34] 3GPP TS38.300. 2018. NR and NG-RAN Overall Description; Stage 2 (Release 15). *V15.2.0 (2018-06)* (2018).
- [35] Baptist Vandersmissen, Nicolas Knudde, Azarakhsh Jalalvand, Ivo Couckuyt, Andre Bourdoux, Wesley De Neve, and Tom Dhaene. 2018. Indoor person identification using a low-power FMCW radar. *IEEE Transactions on Geoscience and Remote Sensing* 56, 7 (2018), 3941–3952.
- [36] IEEE 802.11 working group. 2012. Wireless LAN Medium Access Control (MAC) and Physical Layer (PHY) Specifications Amendment 3: Enhancements for Very High Throughput in the 60 GHz Band. *IEEE Standard 802.11ad* (2012).
- [37] IEEE 802.11 working group. 2019. IEEE Draft Standard for Information Technology-Telecommunications and Information Exchange Between Systems Local and Metropolitan Area Networks-Specific Requirements Part 11: Wireless LAN Medium Access Control (MAC) and Physical Layer (PHY) Specifications-Amendment: Enhanced Throughput for Operation in License-Exempt Bands Above 45 GHz. *IEEE P802.11ay/D3.0* (2019).
- [38] Chenshu Wu, Feng Zhang, Beibei Wang, and KJ Ray Liu. 2020. mmTrack: Passive multi-person localization using commodity millimeter wave radio. In *IEEE INFOCOM 2020-IEEE Conference on Computer Communications*. IEEE, 2400–2409.
- [39] Feng Zhang, Chenshu Wu, Beibei Wang, and KJ Ray Liu. 2020. mmEye: Super-Resolution Millimeter Wave Imaging. *IEEE Internet of Things Journal* (2020).
- [40] Peijun Zhao, Chris Xiaoxuan Lu, Jianan Wang, Changhao Chen, Wei Wang, Niki Trigoni, and Andrew Markham. 2019. mID: Tracking and Identifying People with Millimeter Wave Radar. In *15th International Conference on Distributed Computing in Sensor Systems (DCOSS)*. Santorini Island, Greece.